Juni Khyat (जूनी ख्यात)
(UGC CARE Group I Listed Journal)
ISSN: 2278-4632
Vol-15, Issue-04, No.03, April: 2025

ELECTRIC VEHICLE ON-BOARD CHARGER USING AN ISOLATED MULTIPORT DC-DC CONVERTER

V. Ajay Babu, UG Students, Sree Vahini Institute of Science and Technology (Autonomous), Tiruvuru, A.P
V. Manasa, UG Students, Sree Vahini Institute of Science and Technology (Autonomous), Tiruvuru, A.P
G. Naga Navya, UG Students, Sree Vahini Institute of Science and Technology (Autonomous), Tiruvuru, A.P
S. Santhosh, UG Students, Sree Vahini Institute of Science and Technology (Autonomous), Tiruvuru, A.P
P. Uday Kumar , Assist. Professor, Dept of EEE, Sree Vahini Institute of Science and Technology (Autonomous), Tiruvuru.
Dr.K. KiranKumar, Assoc. Professor, Dept of EEE, Sree Vahini Institute of Science and Technology (Autonomous), Tiruvuru.

ABSTRACT:
An isolated three-port dc–dc converter acts as the basis for the integrated on-board charger (IOBC) for electric vehicles (EVs) as is proposed in the present paper. The proposed configuration offers a reduced component count by combining the auxiliary power module (APM) and on-board charger (OBC) into a single multiport converter. Across the whole battery voltage range, the advised converter can concurrently charge high-voltage (HV) and low-voltage (LV) batteries. Power flow circulates among the three converter ports as a result of galvanic isolation between the ports being provided by a three-winding transformer. In order to control the power flow at the HV and LV ports separately, this paper proposes a unique modulation approach which makes use of the converter's three degrees of freedom (3-DOF) and derives a boundary condition for an initial time. Phase-shifted full-bridge (PSFB) and dual-active-bridge (DAB) converters can potentially be used to charge the LV and HV batteries, respectively. The results demonstrate that, according to the presented 3-DOF selection strategy, all converter semiconductor devices function with zero voltage-switching (ZVS) throughout an extensive power and voltage range without require for further resonant components. The proposed converters MATLAB/Simulink is developed and the results are shown for verification of the ZVS operation and converter analysis
Keywords: phase-shifted full-bridge (PSFB), low-voltage (LV) dc–dc converter, integrated electric vehicle (EV) charger, dual-active-bridge (DAB) converter and three-port converter
.

INTRODUCTION :

Electric vehicles (EVs) are becoming more and more popular as a result of the rising concern about global warming and as such are progressively taking the place of transportation options which rely on fossil fuels. To charge the on-board high-voltage (HV) batteries that drive the electric motor, EVs often feature an on-board charging system that is connected to the utility grid. A low-voltage (LV) battery used to power auxiliary load such lighting, communication, and navigation systems is another feature of EVs. According to current practice, the on-board charging system consists of two distinct dc–dc units, the on-board charger (OBC) and auxiliary power module (APM), which are in charge of charging the HV and LV batteries, respectively, after a front-end active power-factor-correction (APFC) stage [1], [2]. The schematic of a typical OBC and APM design is shown in Fig. 1.1

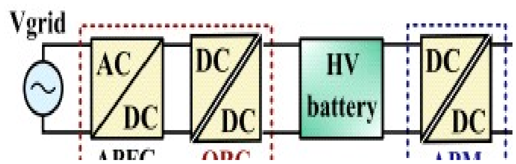

.

Fig.1. Diagram of a traditional OBC-APM system

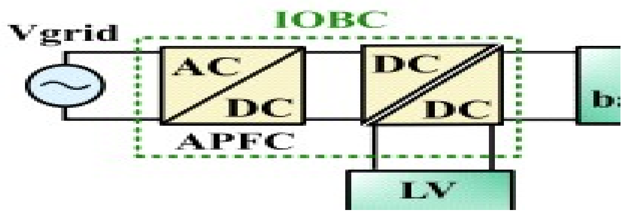

Fig.2. An integrated OBC–APM charger architecture.

The EV charger overall weight, volume, and cost can be greatly decreased, space can be preserved and the EV driving range can be increased with a topological integration of the OBC and APM [3]. Furthermore, by reducing the number of series-connected power processing stages and magnetic components, the integrated charger can accomplish great efficiency. Fig.2 shows the concept of an integrated OBC (IOBC).

ANALYSIS AND OPERATION OF CONVERTERS:

Topology of Converters and Charging Procedures:

Fig. 3 depicts the proposed three-port dc–dc converter architecture. For obtaining galvanic isolation between the ports, a three-winding high-frequency (HF) transformer with a turn ratio of n1: n2: n3 is employed. A front-end PFC stage connects Port 1 to the utility ac grid. Therefore, the PFC step is not covered in this article and the input dc voltage of port 1 or VDC, is regarded as strictly controlled. The HV and LV batteries are connected to ports 2 and 3, respectively, with voltage levels VHV and VLV

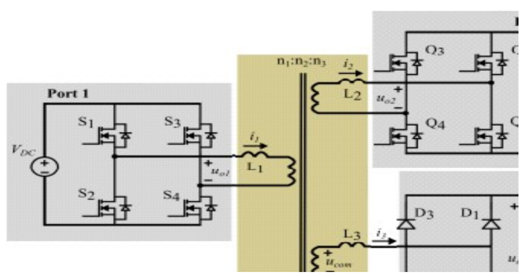

Fig.3. Topology for the integrated converter design.

Ports 1 and 2 are interfaced with the three-winding transformer using H-bridge converters. Therefore, ports 1 and 2 contain the potential to flow electricity in both directions and function as voltage ports. The H-bridge converter produces an HF quasi-square wave voltage, which is represented by the numbers uo1 and uo2 for ports 1 and 2, respectively. As port 3 is coupled to a diode bridge rectifier via an output filter inductor (L f), it functions as a port for unidirectional current. An analogous circuit model, which again neglects the converter magnetizing inductance, can be used to depict the proposed converter shown in Fig. 4.

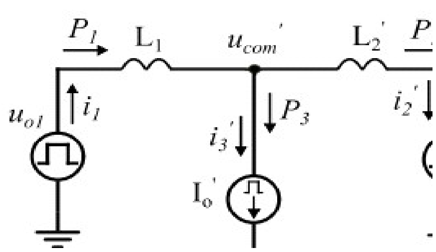

Fig.4. The proposed integrated converter analogous circuit design

The following factors being taken into consideration for the analogous circuit model of Fig. 4.
The power flow equations for this converter are mutually linked as a result of the multi winding transformer usage, increasing the complexity of control [28]. In order to regulate power flow at ports 2 and 3, a unique modulation technique is proposed in this paper. Similar to a DAB converter, power flow between ports 1 and 2 can be managed, whereas PSFB converter control can be used to manage power flow to port 3. For the HV and LV batteries to be charged simultaneously and for each battery charging to be independently controlled, the proposed modulation method is necessary.

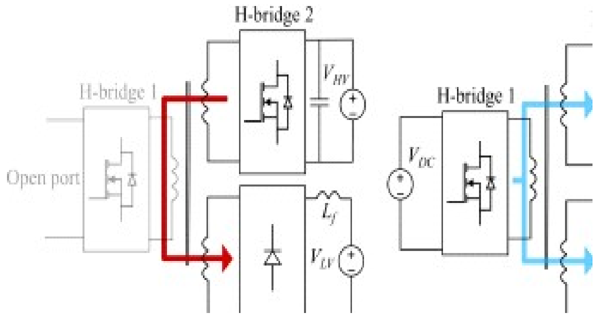

Fig.5. The proposed integrated charger charging features. (a) Charging batteries from HV to LV. (b) Grid-based synchronized LV and HV battery charging.

STEADY STATE ANALYSIS AND MODULATION TECHNIQUE FOR CONVERTERS :
The semiconductor switches of the main and secondary H-bridge converters gate signals are displayed in Fig. 6 (a). Along with the current waveforms of the primary and secondary transformer windings, i1 and i2, Fig. 6 (b) and (c) reveal the applied voltages at the transformer primary and secondary windings, io1 and uo2, which are produced in accordance with these gate signals. The voltage induced at the transformer low voltage winding, or ucom, and the corresponding winding current, or i3, are displayed in Fig. 6(d). φ represents the phase shift between the basic components of uo1 and uo2 and τ 1 and τ 2 represent the pulse lengths of uo1 and uo2, respectively, applied voltages. Fig.6 (b) and (c) demonstrate that the suggested converter provides 3-DOF, i.e., φ, τ 1, and τ 2.
First, as shown in the corresponding model of Fig. 4, the tertiary winding leakage inductance, or L3, has been disregarded. Therefore, the commutation effect caused by L3 in the port 3 diode bridge is not taken into account. Finally, because of the huge output filter inductor, Lf, the output current ripple, i.e., ILV, is regarded as insignificant.

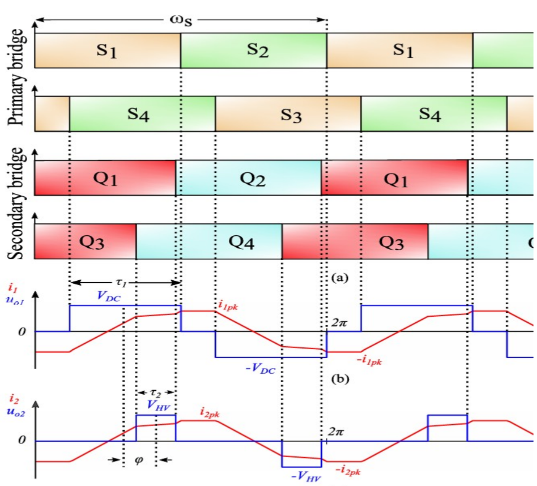

Fig.6. (a) Gate signals of semiconductor switches S1–S4 and Q1–Q4. (b) Primary, (c) secondary, and (d) tertiary winding voltage and current waveforms with 3-DOF converter operation.

Ucom is a multilayer waveform that arises from the superposition of the applied voltages at the transformer's main and secondary windings at each moment in time, as seen in Fig. 6(d). The basic ucom, or u ′ com, can be defined as follows using the superposition theorem on the analogous circuit model of Fig. 4.

$$u'_{com}(t) = \frac{L'_2}{L_1+L'_2}u'_{01}(t) + \frac{L_1}{L_1+L'_2}u'_{02}(t) \quad \ldots\ldots\ldots \qquad (1)$$

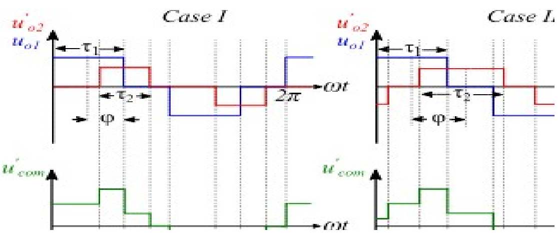

Fig.7 Two distinct examples of uo1 and u ′ o2, the tertiary winding generated voltage is referred to as primary, i.e., u ′ com.

$$\emptyset + \frac{\tau_1}{2} + \frac{\tau_2}{2} \le \pi. \qquad (2)$$

Case I: $V_{LV} = \frac{n_3}{n_1}\frac{2L'_2}{L_1+L'_2}d_1V_{DC} + \frac{n_3}{n_2}\frac{2L_1}{L_1+L'_2}d_2V_{HV}$ (3)

Case: II $V_{LV} = \frac{n_3}{n_1}\frac{2L'_2}{L_1+L'_2}d_1V_{DC} + \frac{n_3}{n_2}\frac{2L_1}{L_1+L'_2}yV_{HV}$ (4)

where d1 = (τ1/2π), d2 = (τ2/2π), and y = (1−d1− (φ/π)). The 3-DOF, i.e., φ, τ1, and τ2 can be selected in the range of 0 < φ ≤ (π/2), 0 < τ1 ≤ π, and 0 < τ2 ≤ π and consequently, 0 < d1 ≤ 0.5 and 0 < d2 ≤ 0.5. Equations (3) and (4) show that in the first case, mean output voltage

$$u_{01}(t) = \sum_{n=1,3,5,\ldots}^{\infty} \frac{4V_{DC}}{n\pi}\cos\left(\frac{n\alpha_1}{2}\right)\sin(n\omega_s t) \qquad (5)$$

$$u_{02}(t) = \sum_{n=1,3,5,\ldots}^{\infty} \frac{4V_{HV}}{n\pi}\cos\left(\frac{n\alpha_2}{2}\right)\sin(n\omega_s t + n\emptyset) \qquad (6)$$

where α1 = π − τ1, α2 = π − τ2, ωs = 2π fs, fs is the converter switching frequency, and n indicates the order of harmonic components. The power flow equations as shown below are subsequently calculated using the applicable model of Fig. 4 [34].

$$P_1 = P_2 + P_3 \qquad (7)$$

$$P_2 = \sum_{n=1,3,5,\ldots}^{\infty} \frac{8V_{DC}V'_{HV}\cos\frac{n\alpha_1}{2}\cos\frac{n\alpha_2}{2}}{\pi^2 n^3 X_{eq}}\sin(n\emptyset) \qquad (8)$$

$$P_3 = V_{LV}I_{LV} \qquad (9)$$

where Xeq = ωs (L1 + L ′ 2), which represents the equivalent impedance between ports 1 and 2. Equation (8) suggests that power at port 2 is a function of all 3-DOF, i.e., P2 = f (φ, τ1, τ2). Furthermore, in accordance with (9), adapting the corresponding port output voltage, or VLV, will enable the necessary power at port 3.

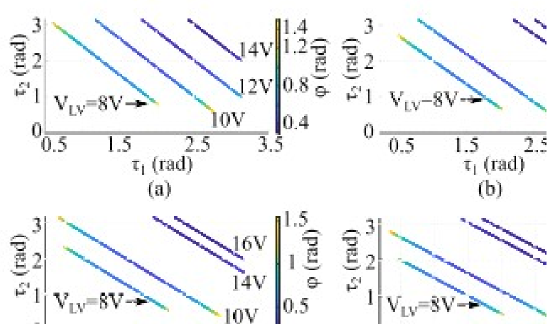

Fig.8. 3-DOF region for Case I operation and LV battery voltage variation with VDC = 400 V, P2 = 3 kW, and P3 = 0.5 kW. (a) VHV = 250 V. (b) VHV = 300 V. (c) VHV = 350 V. (d) VHV = 400 V.

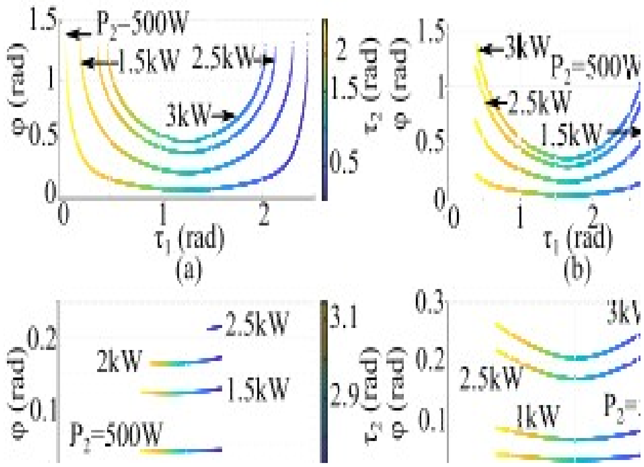

Fig.9. 3-DOF area for Case I operation and port 2 power variation with VDC = 400 V and P3 = 0.5 kW. (a) VHV = 400 V and VLV = 8 V. (b) VHV = 350 V and VLV = 10 V. (c) VHV = 280 V and VLV = 16 V. (d) VHV = 400 V and VLV = 16 V.

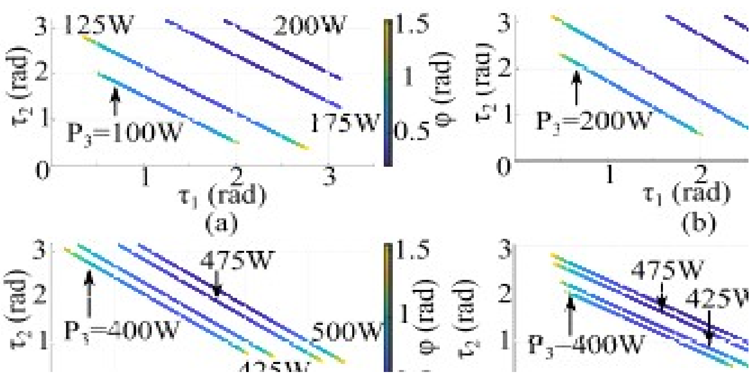

Fig.10. 3-DOF region for Case I operation and port 3 power variation with VDC = 400 V and P2 = 3 kW. (a) VHV = 400 V and ILV = 12.5 A. (b) VHV = 350 V and ILV = 25 A. (c) VHV = 250 V and ILV = 50 A. (d) VHV = 400 V and ILV = 50 A.

Table-I

Boundary conditions for each mode of operation

Mode	Boundary conditions
Ia	$\emptyset > 0, \tau_1 \geq \tau_2, \emptyset - \frac{\tau_1}{2} + \frac{\tau_2}{2} > 0, -\emptyset + \frac{\tau_1}{2} + \frac{\tau_2}{2} > 0$
Ib	$\emptyset > 0, \tau_1 \geq \tau_2, \emptyset - \frac{\tau_1}{2} + \frac{\tau_2}{2} > 0, -\emptyset + \frac{\tau_1}{2} + \frac{\tau_2}{2} > 0$
II	$\emptyset > 0, \tau_1 \geq \tau_2, -\emptyset + \frac{\tau_1}{2} + \frac{\tau_2}{2} > 0$
III	$\emptyset > 0, \tau_1 \geq \tau_2, -\emptyset - \frac{\tau_1}{2} + \frac{\tau_2}{2} > 0$
IV	$\emptyset > 0, \emptyset - \frac{\tau_1}{2} + \frac{\tau_2}{2} > 0$

MODES OF OPERATION FOR CONVERTERS:

The ac voltages produced at each H-bridge converter output, i.e., uo1 and uo2, can produce a variety of voltage patterns based on the rising and falling edges of uo1 and uo2, reminiscent of a DAB converter [35]. Five modes of operation are discovered for sets of φ, τ1 and τ2,

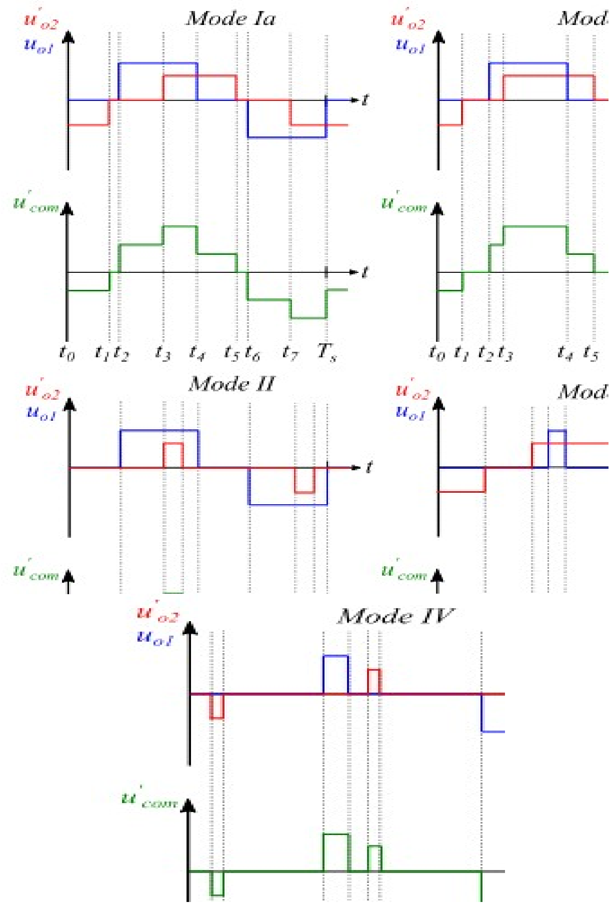

Fig.11. The proposed converter modes of operation for Case I

The five operating modes boundary conditions are shown in Table I. As can be observed, Mode I is divided into two categories: Mode Ia and Mode Ib

$$P_2 = \frac{V_{DC}V_{HV}}{\omega L}\varphi\left(1-\frac{\varphi}{\pi}\right) \leq 3KW \Rightarrow L \leq 61.67\mu H \quad (10)$$

where the greatest P2 is obtained by using $\varphi = (\pi/2)$.

A particular ratio of L1 to L′ 2 is not necessary for a suggested converter to function, while (10), on the other hand, establishes a maximum limit for L1 + L′ 2

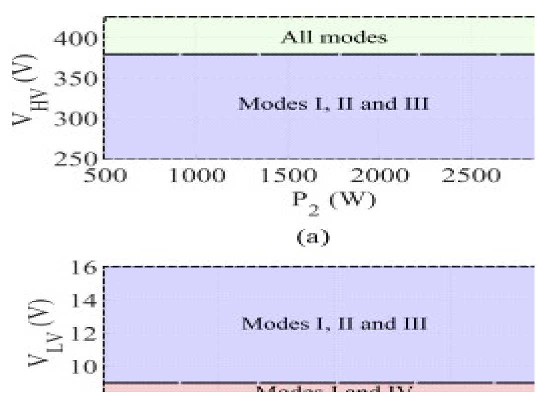

Fig.12. Boundaries of each mode of operation for (a) 250 V ≤ VHV ≤ 420 V, VLV = 10 V, and P3 = 500 W and (b) 8 V ≤ VLV ≤ 16 V, 100 W ≤ P3 ≤ 500 W, VHV = 370 V, and P2 = 3KW.

Table- II

ZVS switching requirement for S1, S4, Q1 and Q4

Device	ZVS condition
S1	$i_{D,s1}(t_j) = i_1(t_j) < 0$
S2	$i_{D,s4}(t_j) = i_1(t_j) < 0$
Q1	$i_{D,Q1}(t_k) = -i_2(t_k) < 0$
Q4	$i_{D,Q4}(t_l) = -i_2(t_l) < 0$

Fig. 12(a) shows that Mode IV cannot be utilized to provide the required P2 when VHV is less than 380 V, VLV = 10 V, and P3 = 500 W. Moreover, Modes I–III can be used when VHV = 370 V, P2 = 3 kW, and VLV > 9 V, whereas Modes I and IV can be used when VHV = 370 V, P2 = 3 kW, and VLV > 9 V, as seen in Fig.12(b).

ZVS EVALUATION OF THE CONVERTER:

It is important to glance at the suggested converter soft-switching features, particularly the switches ZVS turn-on capability. The polarity of the switch current at each semiconductor device switching moment needs to be ascertained. The analogous switch of the corresponding **V.**

SELECTION OF FUNCTION MODES:

According to Figs. 8–10, the converter can perform with a variety of φ, τ1 and τ2 configurations at a given functioning point, which includes allocated port voltage levels and power needs. Each pair of [φ τ1 τ2] denotes one of the five stages of Case I converter operation seen in Fig. 11. The converter area for Case I at four distinct operating points is depicted in Fig.13. Adjustments in VHV, VLV, P2 and P3 were each placed into consideration and the associated converter mode of operation is indicated by a color.

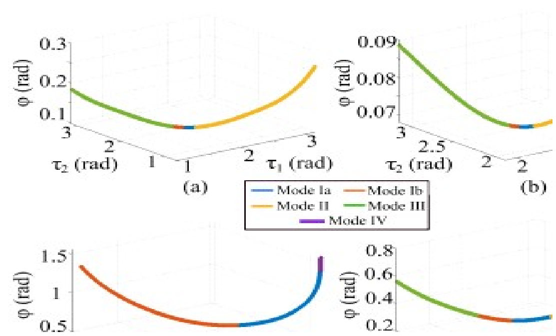

Fig.13. Converter region and functioning modes for (a) VHV = 350 V, VLV = 12 V, P2 = 1 kW and P3 = 200 W, (b) VHV = 400 V, VLV = 16 V, P2 = 1 kW and P3 = 200 W, (c) VHV = 250 V, VLV = 8 V, P2 = 3 kW and P3 = 500 W and (d) VHV = 350 V, VLV = 12 V, P2 = 3 kW and P3 = 500 W.

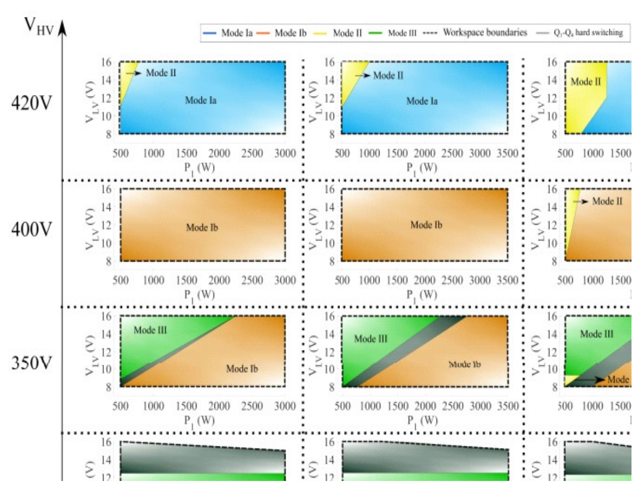

Fig.14. ZVS range of the proposed converter for 8 V ≤ VLV ≤ 16 V, P1 in the range 0.5 kW ≤ P1 ≤ 3.5 kW, VHV = 250, 350, 400, and 420 V, and three distinct relationships between P2 and P3, that is: 1) P2 = P1 − P3 and P3 = 50 W; 2) P2 = P1 − P3 and P3 = 450 W; and 3) P2 = (6/7) P1 and P3 = (1/7) P1.

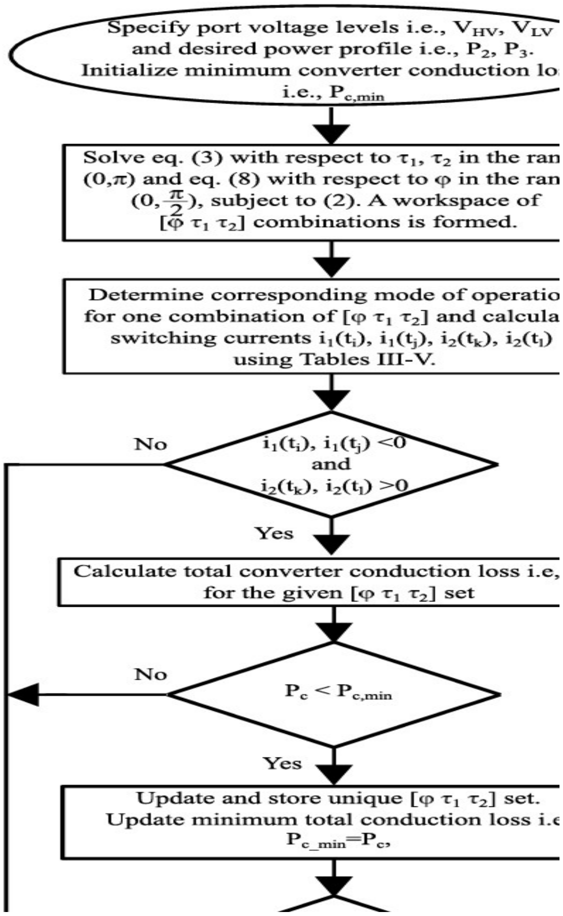

Fig.15. Flowchart of the unique [φ τ1 τ2] parameters selection for given converter operating conditions.

CONSTANT VOLTAGE AND CONSTANT CURRENT CHARGING:

The suggested integrated charger uses a constant-voltage (CV) and constant-current (CC) charging system [38]. The CC/CV charging scheme design, which is clarified below, is comparable for both LV and HV batteries.

LV Table- III

CC and CV charging parameters for the LV and hv batteries

Parameters	C	HV battery	LV battery
CC mode operating	-	250V-370V	8V-10V
CV mode operating	-	370V-420V	10V-16V
CC/CV mode transition	$V_{x,crit}$	370V	10V
CC mode charging	$I_{x,CC}$	8.1A	50A

In conformity with the flowchart in Fig.15, the distinct combinations of the converter 3-DOF, namely φ, τ1, and τ2, are computed earlier for certain operating points combination.

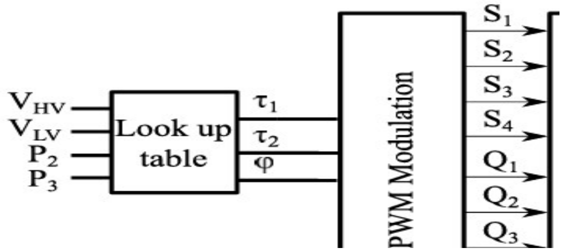

Fig.16. CC and CV charging scheme of the proposed integrated charger using lookup table.

SIMULATION RESULTS:

For simultaneous HV and LV battery charging operation using the CC/CV charging scheme, the converter is simulated using PLECS software. Table IV lists all the ideal components and characteristics.

Description	Port 1	Port 2	Port 3
Voltage level (V)	400	250-420	8-16
Nominal power (kw)	3.5	3	0.5
Leakage inductance (µH)	6.67	6.67	6.67
Switching frequency (KHZ)		100	

In the CC charging zone, the converter 3-DOF and the voltage and current waveforms of the HV and LV batteries are displayed in Fig. 17. both batteries with CC, while VHV and VLV are continually increasing.

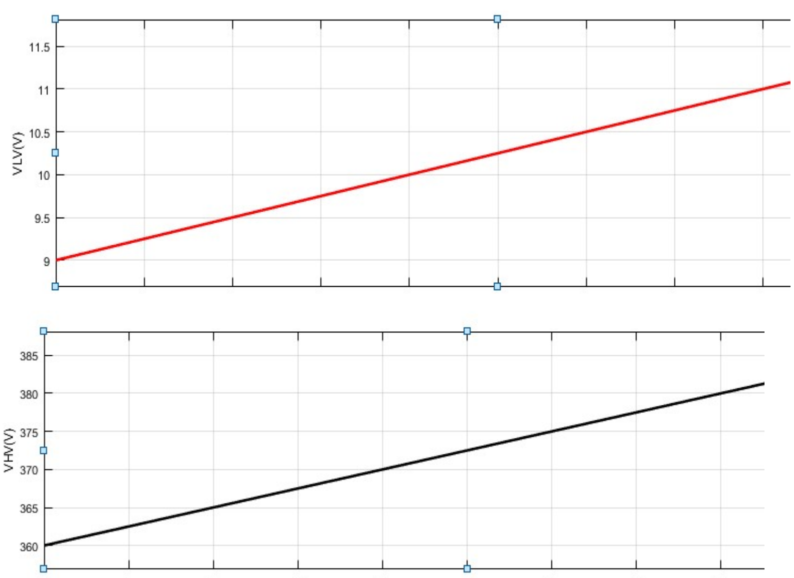

The transformer is functioning in Mode Ib at nominal voltage and power levels, according to the transformer voltage and current waveforms displayed in Fig. 18. According to Table VI ZVS requirements, all of the active devices of the suggested converter run with ZVS for the nominal operating points of VHV = 370 V, VLV = 10 V, P2 = 3 kW and P3 = 500 W. Also, the device turn-on currents are reflected through the corresponding transformer winding

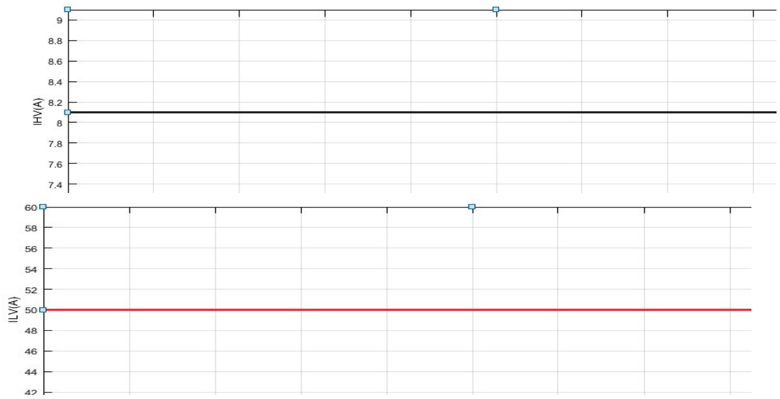

(a)

Fig.17. (a) Voltage and current waveforms of the HV and LV batteries

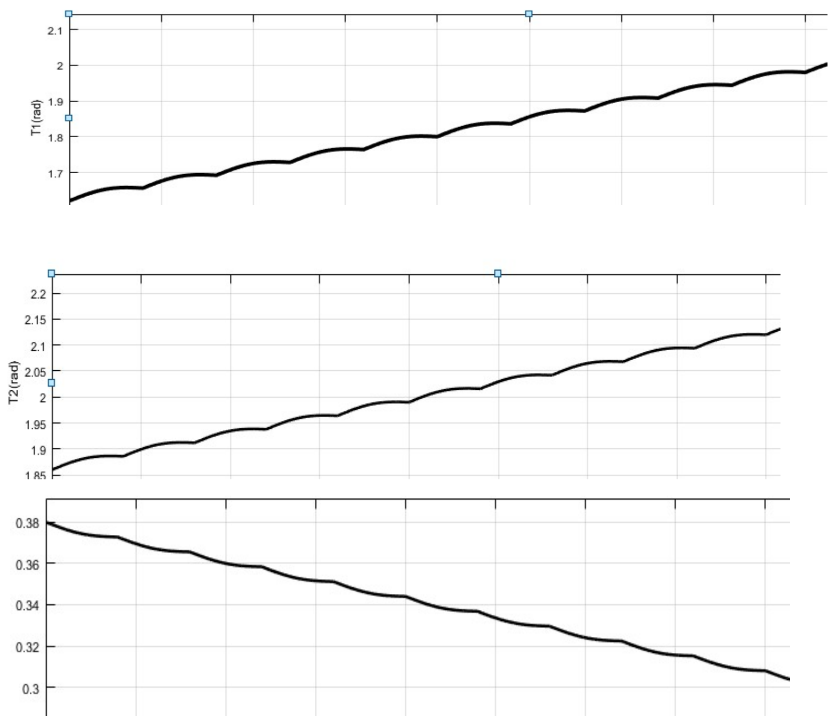

(b) Converter 3-DOF during CC charging of the HV and LV batteries.

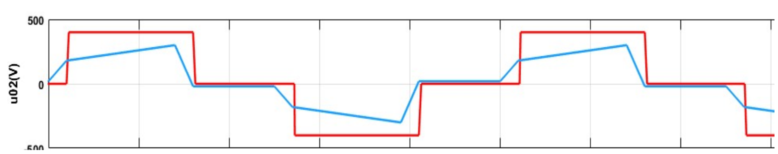

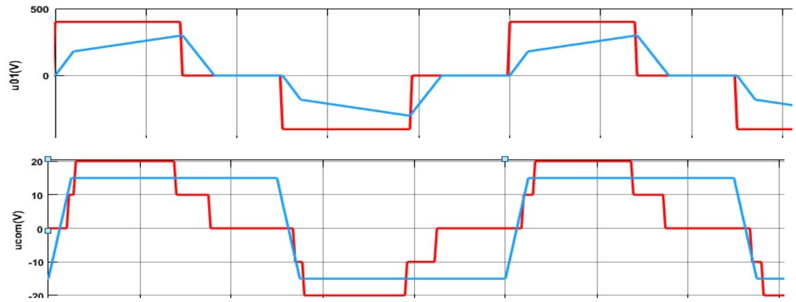

Fig.18. Transformer voltage and current waveforms for nominal power operation in Mode Ib with VDC = 400 V, VHV = 370 V, VLV = 10 V, P2 = 3kW, and P3 = 500 W.

The transformer voltage and current waveforms throughout the CV charging period are finally displayed in Fig.20, where it is clear that the converter first functions in Mode Ia and then in Mode II. All converter devices are confirmed to function with ZVS for both Modes Ia and II operation by looking at the polarity of the main and secondary winding currents during the device turn-on instances. The latter is in line with Fig.

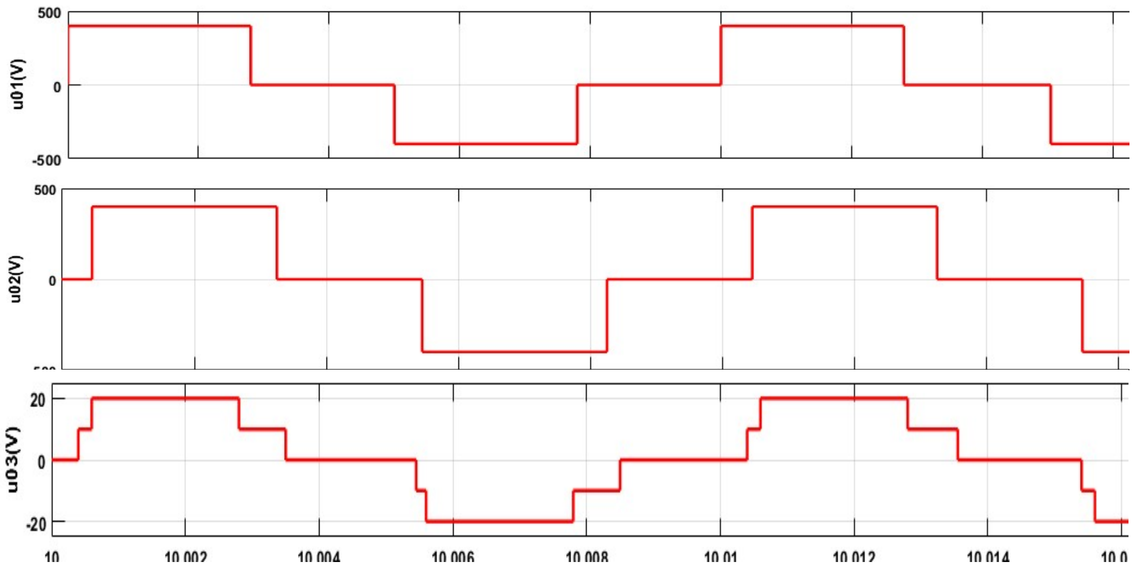

(a)

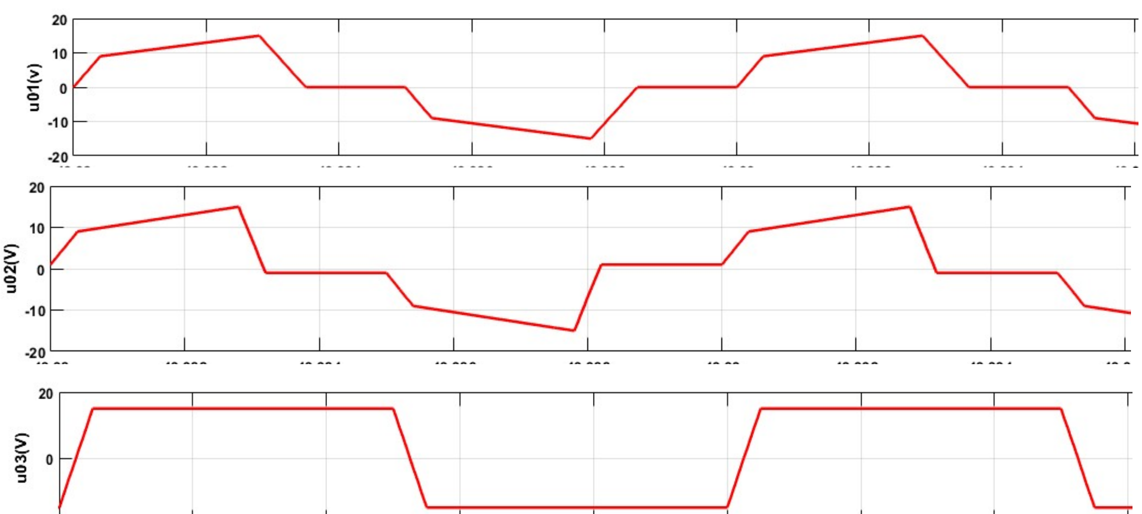

(b)

Fig.20. Transformer voltage and current waveforms during CV charging of the HV and LV batteries and converter operation in (a) Mode Ia and (b) Mode II.

CONCLUSION:

In this paper, a three-port isolated dc-dc converter has been introduced and examined. The advised converter functions across a broad voltage range and can concurrently charge both HV and LV batteries, thus being appropriate for OBC and APM integration in the EV powertrain. Furthermore, neither relays nor mechanical switches are used by the specified converter. When isolation criteria are fulfilled, a single three-winding transformer is used, which lowers the volume and cost of the magnetics in comparison to using separate two-winding transformers. To enable the HV and LV batteries to be charged independently, a new modulation technique and a boundary condition are being developed to decouple the power flow between the converter three ports. Furthermore, ZVS is attained for all of the converter active devices throughout a broad power and voltage range due to a proposed 3-DOF selection technique, which eliminates the requirement for extra resonant components. A SiC MOSFET converter simulation results demonstrated the efficacy of the proposed converter for upcoming integrated OBC applications.

REFERENCES

[1] J. Yuan, L. Dorn-Gomba, A. D. Callegaro, J. Reimers, and A. Emadi, “A review of bidirectional on-board chargers for electric vehicles,” IEEE Access, vol. 9, pp. 51501–51518, 2021.

[2] H. V. Nguyen, D. Lee, and F. Blaabjerg, “A novel SiC-based multifunctional onboard battery charger for plug-in electric vehicles,” IEEE Trans. Power Electron., vol. 36, no. 5, pp. 5635–5646, May 2021.

[3] G. Yu and S. Choi, “An effective integration of APM and OBC with simultaneous operation and entire ZVS range for electric vehicle,” IEEE Trans. Power Electron., vol. 36, no. 9, pp. 10343–10354, Sep. 2021.

[4] L. Zhu, H. Bai, A. Brown, and L. Keuck, “A current-fed three-port DC/DC converter forintegration of on-board charger and auxiliary power module in electric vehicles,” in Proc. IEEE Appl. Power Electron. Conf. Expo. (APEC), Jun. 2021, pp. 577–582.

[5]S. Dey and A. Mallik, “Multivariable-Modulation-Based conduction loss minimization in a triple-active-bridge converter,” IEEE Trans. Power Electron., vol. 37, no. 6, pp. 6599–6612, Jun. 2022.

[6] N. D. Dao, D. Lee, and Q. D. Phan, “High-efficiency SiC-based isolated three-port DC/DC converters for hybrid charging stations,” IEEE Trans. Power Electron., vol. 35, no. 10, pp. 10455–10465, Oct. 2020.

[7] Z. Lin et al., “A three-port LCC resonant converter for the 380-V/48-V hybrid DC system,” IEEE Trans. Power Electron., vol. 37, no. 9, pp. 10864–10876, Sep. 2022.

[8] R. Erickson and D. Maksimovic, Fundamentals of Power Electronics. Cham, Switzerland: Springer, 2020, doi: 10.1007/978-3-030-43881-4.

[9] S. Bandyopadhyay, P. Purgat, Z. Qin, and P. Bauer, “A multiactive bridge converter with inherently decoupled power flows,” IEEE Trans. Power Electron., vol. 36, no. 2, pp. 2231–2245, Feb. 2021.

[10] P. Purgat, S. Bandyopadhyay, Z. Qin, and P. Bauer, “Zero voltage switching criteria of triple active bridge converter,” IEEE Trans. Power Electron., vol. 36, no. 5, pp. 5425–5439, May 2021.